Water Research 190 (2021) 116720

Contents lists available at ScienceDirect

Water Research

journal homepage: www.elsevier.com/locate/watres

Near-infrared light to heat conversion in peroxydisulfate activation with MoS_2: A new photo-activation process for water treatment

Renli Yin[a], Binghua Jing[b], Shaoxiong He[a], Jiayue Hu[a], Gang Lu[a], Zhimin Ao[b,*], Chuanyi Wang[c], Mingshan Zhu[a,*]

[a] Guangdong Key Laboratory of Environmental Pollution and Health, School of Environment, Jinan University, Guangzhou 511443, China
[b] Guangdong Key Laboratory of Environmental Catalysis and Health Risk Control, Guangzhou Key Laboratory Environmental Catalysis and Pollution Control, School of Environmental Science and Engineering, Institute of Environmental Health and Pollution Control, Guangdong University of Technology, Guangzhou 510006, China
[c] School of Environmental Science and Engineering, Shaanxi University of Science and Technology, Xian 710021, China

ARTICLE INFO

Article history:
Received 15 September 2020
Revised 24 November 2020
Accepted 1 December 2020
Available online 2 December 2020

Keywords:
Light-to-heat conversion
Peroxydisulfate
Near-infrared light
MoS_2
Membrane

ABSTRACT

The advantage of light-to-heat conversion can be employed as an optical alternative for environmental remediation. As a proof of concept, for the first time we introduce the light-to-heat conversion application in peroxydisulfate (PDS) activation by molybdenum disulphide (MoS_2) under near infrared (NIR) light irradiation. Theoretical kinetics analysis suggests that the reaction rates of PDS activation is increased up to 9.2 times when increasing from room temperature to 50 °C. MoS_2 has the capability to quickly convert NIR light to heat energy (~45°C), thereby being able to activate PDS to generate hydroxyl and sulfate radicals. The observed reaction rate of carbamazepine degradation by NIR/MoS_2/PDS process is 6.5 times of that in MoS_2/PDS and even 2.6 times higher than the sum of those in NIR/MoS_2, MoS_2/PDS and NIR/PDS processes. Combining with theoretical calculation and oxidation species analysis, a new photo-activation PDS mechanism is proposed, in which MoS_2 absorbs the energy of light to generate heat energy for overcoming the energy barrier of PDS activation. By loading MoS_2 on carbon cloths, a flexible photothermal membrane is designed for practical application of sunlight-to-heat conversion to activate PDS with high efficiency, stability, and recycling. The present results demonstrate the potential of applying light-to-heat conversion in Fenton-like processes in pollution control, which opens new avenues towards utilization of inexhaustible solar energy and novel approaches for environmental remediation.

1. Introduction

Advanced oxidation processes (AOPs), like Fenton, ozone, and persulfate, etc., can *in situ* produce highly reactive radicals (•OH and $SO_4^{\bullet-}$) to abate a wide range of organic pollutants in water, which has attracted great interests among researchers in recent decades (Hodges et al. 2018). Among these AOPs, peroxydisulfate (PDS)-based AOPs not only overcome the potential dangers of O_3 and H_2O_2 during use and transportation, but also generate the radicals of $SO_4^{\bullet-}$, which exhibits stronger oxidizing capability ($E^0(SO_4^{\bullet-}/SO_4^{2-})$ = 2.5–3.0 V) at a wide pH range (3–9) (Niu et al. 2020, Yin et al. 2019). Furthermore, in comparison with other traditional oxidants including H_2O_2, O_3, potassium ferrate, and peroxymonosulfate (PMS), PDS has following advantages: the cheapest price with same quality; the longest lifetime in water, and the lowest activation energy (**Table S1**) (Wacławek et al. 2017, Yin et al. 2020). Thus PDS is capable of degrading highly toxic and persistent pollutants and is the first choice for *in situ* chemical oxidation (ISCO) treatment for water or soil (Avetta et al. 2015, Chu et al. 2019, Kang et al. 2019, Ke et al. 2019, Zheng et al. 2019).

Generally, PDS can be physically activated by external energy (including UV, heat and ultrasound, (Eq. (1))) or chemically activated by transition metals or chemical activation agents (Eq. (2)) to generate $SO_4^{\bullet-}$ (Duan et al. 2018, Nie et al. 2019, Yin et al. 2018, Zhou et al. 2019). Compare with the chemical activation of PDS to generate one mole of $SO_4^{\bullet-}$ for each mole PDS, the physical activation pathway results in the symmetrical cleavage of the peroxide bond results in yielding stoichiometrically two moles of $SO_4^{\bullet-}$ for the decomposition of each mole PDS, which minimizes the consumption of PDS and avoids the metal leaching to cause secondary contamination (Lee et al. 2020). However, the physical activation are generated from the external energy such as electrical energy.

* Corresponding author.
E-mail addresses: zhimin.ao@gdut.edu.cn (Z. Ao), zhumingshan@jnu.edu.cn (M. Zhu).

https://doi.org/10.1016/j.watres.2020.116720
0043-1354/

These multiple transformations bring energy loss as well as high cost. Thus from economic and environmentally friendly viewpoints, a green and sustainable method yet highly efficient is required for the activation of PDS.

$$S_2O_8^{2-} + external energy (heat, ultrasound, and UV) \rightarrow 2SO_4^{\bullet -} \quad (1)$$

$$S_2O_8^{2-} + e^- \rightarrow SO_4^{\bullet -} + SO_4^{2-} \quad (2)$$

Solar energy is the free, cleanest and most abundant renewable energy source. Recently, tremendous advances have been made in the photo-activated PDS by using UV- or visible light-driven photocatalytic techniques. In the solar radiation spectrum, UV light, visible light, and near infrared (NIR) light are account for ca. 5%, 48%, and 44%, respectively (Liu et al. 2016). Many of the researches concentrate on exploring the photo-involved reactions in the UV or visible light (less than 600 nm) region, while ignore the half solar energy, the NIR region. This is because most of photo-involved reactions can not be driven by NIR. Moreover, NIR energy always brings strong thermal effects during photo-involved reactions while the researchers try a lot of ways to avoid this thermal effect. However, is it possible to utilize the thermal effect caused by NIR energy for the activation of PDS in environmental application based on the fact that PDS can be thermally activated (Fan et al. 2015, Waldemer et al. 2007)?

As is known, light-to-heat conversion, harvesting and converting solar irradiation by photothermal materials into heat for beneficial usage, has diversely applied in cancer therapy, solar power generation, and seawater desalination, as well as in some environmental applications (Li et al. 2017, Wang et al. 2017). For instance, the hybrid nanomaterial Pt-rGO-TiO_2, featuring the broad light wavelength absorption (800–2500 nm), was reported to be a highly active photo-thermal responsive catalyst for efficient VOCs decomposition under NIR irradiation (Li et al. 2018). The photothermal materials could efficiently absorb the energy of light, resulting in light-to-heat conversion, thereby increasing reaction temperature. When the temperature increases above the light-off temperature for the thermocatalytic oxidation, the thermocatalytic oxidation reaction can take place. For instance, Fan et al found that, as the temperature increased from 40 to 60 °C, the removal rate of sulfamethazine increased from 20% to 70%, of which the value of k_{obs} increased by 21-fold (Fan et al. 2015). Thus the light-to-heat conversion would be an optical alternative for PDS activation process. As far as we known, there is a big knowledge gap in the understanding of the light-to-heat conversion method for PDS activation for environmental remediation, which provides a new way for the elimination of requirement on thermal energy from fossil-derived fuels. Therefore, it is of great importance and challenge to explore the potential of NIR-driven light-to-heat conversion application in PDS activation, which promotes the utilization of solar energy and opens the possibility of substituting light-to-heat catalytic reactions for conventional thermalcatalytic redox reactions based on heat from fossil-derived fuels.

For the first time, we introduce the light-to-heat conversion application in PDS activation under NIR irradiation in this work. Herein, molybdenum disulphide (MoS_2), a typical photo-thermal material (Chou et al. 2013, Liu et al. 2014), is adopted to testify the potential of light-to-heat conversion in PDS activation, while the carbamazepine (CBZ, an antiepileptic drug and persistent organic micropollutant) is chosen as the target pollutant. Remarkably, the reaction solution temperature increased up to 45 °C under the irradiation of a 808 nm laser, in which the localized heat converted from light energy directly activate PDS to enhance the removal efficiency of CBZ. Based on both the experimental and theoretical evidence, we reveal that the highly efficient catalytic activity originates from solar light-driven thermocatalysis that was considerably enhanced by a conceptually novel photoactivation effect different from conventional photocatalysis. This work highlights that the light-to-heat conversion shows promise for redox catalysis applications, which will open new avenues toward the utilization of inexhaustible solar energy for environmental remediation.

2. Materials and methods

2.1. Chemicals and Reagents

A detailed list of chemicals and reagents is provided in Text S1 in the Supporting Information.

2.2. Synthesis of MoS_2 nanosheets and membrane

MoS_2 nanosheets were synthesized by a facile hydrothermal method. 0.25 mmol of $(NH_4)_6Mo_7O_{24}\bullet 4H_2O$ and 0.75 mmol of CH_4N_2S were added into the water-ethanol mixtures (V_{water}:$V_{ethanol}$=5:1) with ultrasonication for 1 h. Then, the homogeneous solution was transferred into a 100 mL Teflon autoclave and kept at a temperature of 210°C for 24 h. After that, the obtained black precipitates were collected by centrifugation and washed with deionized water and ethanol for 3 times, respectively, and then dried in an oven at 60°C for 12 h. To reuse the catalysts easily, the MoS_2 nanosheets were grown on the highly flexible surface of carbon cloth (CC) with diameter of 5 cm to form a CC/MoS_2 membrane. The CC/MoS_2 membrane was formed corresponding to the preparation of MoS_2 by adding external CC as the precursor.

2.3. Characterization

UV-visible-NIR diffuse reflectance spectra (UV-vis-NIR-DRS, JASCO V-770) of MoS_2 were obtained with $BaSO_4$ used as a reflectance standard. X-ray diffraction (XRD) pattern was analyzed using a D5000, Siemens (Germany), including a Cu Kα exciting source (λ=1.54056 Å). A transmission electron microscope (TEM), Hitachi H-7650 at accelerating voltage 100 kV, was applied to characterize the catalyst morphologies. X-ray photoelectron microscopy (XPS) was conducted on a Thermo Escalab 250 using an Al Kα X-ray source. Electron paramagnetic resonance (EPR) experiments were monitored using an EMX-8/2.7 spectrometer (Bruker, Germany).

2.4. Experimental procedures

A 2 W 808 nm portable infrared laser (Highlasers, HK) was used as light source for 808 nm laser as NIR light for PDS activation. Batch tests of CBZ degradation were carried out in the brown quartz bottle with 2.0 mL solution on magnetic stirrers. First, MoS_2 was added into the solution with CBZ and stirred for 30 min to achieve adsorption equilibrium. Then, the activation process was initiated by adding a certain amount of PDS and turning on the NIR light to the solution. Each experiment was done in duplicate to calculate the average values for reproducibility, while the standard deviation of the values was calculated to draw the error bar. The experiments were conducted at the initial CBZ concentration of 10 mg L^{-1}, PDS concentration of 2.0 g L^{-1}, MoS_2 concentration of 1.0 g L^{-1}, and pH of 5.0, while the distance between the light and the bottle was 2.0 cm. 0.10 mL of the reaction solution was withdrawn at given time and immediately quenched and diluted then filtered into a vial for analysis. While experimental conditions of the sunlight-to-heat conversion in outdoor conditions: LI=50 mW cm^{-2}, [pollutants] = 10 mg L^{-1}, $[PDS]_0$=2.0 g L^{-1}, volume = 20 mL, T = 30°C. High-performance liquid chromatography (HPLC, Shimadzu, LC-16) equipped with an Agilent SB–C18 column (2.1 mm×100 mm, 1.8 μm) was used to observe the concentration

of CBZ, the UV detector was set at 285 nm. The mobile phase consists of 30% acetonitrile and 70% 0.10% formic acid with the flow rate of 0.20 mL min^{-1}.

2.5. Computational methods

All calculations were performed in DMol^3 code, which is based on first-principle quantum mechanics (Ao et al. 2008, Delley 1990, 2000, Segall et al. 2002). Generalized gradient approximation (GGA) with Perdew-Burke-Ernzerhof (PBE) method was used as the exchange-correlation function (Hammer et al. 1999, Liao et al. 2012, Perdew et al. 1996). Spin-polarization was included in all calculations and a damped van der Waals correction was incorporated using Grimme's scheme to describe the non-bonding interactions (Du et al. 2012). The *k*-point sampled the irreducible wedge of the Brillouin zone, was increased until the calculated energy converges within the required tolerance (Ao et al. 2009). In this work, *k*-point was set to 5×5×1 for all slabs, which has an energy convergence tolerance of 1×10^{-5} Ha/atom for SCF (self-consistent filed) procedure with a maximum force of 0.002 Ha/Å. 4.9 Å global orbital cutoff were used in all calculations. In order to better simulate the experimental environment, water solvation model (COSMO) with a dielectric constant of 78.54 was used during all the calculations to mimic the aqueous condition. In addition, the calculations on systems including PDS were given charge -2|e| to consider the charge state of $S_2O_8^{2-}$.

In the simulation, a single layer 4×4×1 supercell of MoS_2 with a vacuum width of 30 Å was constructed to ensure the interaction between the repeated slabs along the normal of surface as weak as possible (Ao et al. 2009). All atoms were allowed to relax for all energy calculation. The favorable structure of $S_2O_8^{2-}$ adsorption on MoS_2 for calculations is shown in Fig. S1(a), while Fig. S1(b) is the band structure of pristine MoS_2. The bandgap E_g is 1.747 eV, which is consistent to the reported experiment result of 1.595 eV and 1.60-2.07 eV (Mombrú et al. 2018, Zhao et al. 2018).

Based on DFT calculations, the results of vibrational analysis or Hessian evaluation can be used to calculate enthalpy (*H*), entropy (*S*), Gibbs free energy (*G*), and heat capacity at a constant pressure as a function of temperature (*T*). Thus, Gibbs free energy of the system before and after adsorption can be obtained. The difference of Gibbs free energy in $S_2O_8^{2-}$ adsorption ($\Delta G_{adsorption}$) can be expressed as:

$$\Delta G_{adsorption}(T) = G_{MoS_2-S_2O_8^{2-}}(T) - G_{MoS_2}(T) - G_{S_2O_8^{2-}}(T), \quad (3)$$

while the $S_2O_8^{2-}$ activation process of Gibbs free energy difference ($\Delta G_{activation}$) could be determined by eq. (4):

$$\Delta G_{activation}(T) = G_{FS}(T) - G_{IS}(T) \quad (4)$$

where $G_{FS}(T)$ and $G_{IS}(T)$ are respectively the corresponding Gibbs free energies of FS and IS configurations in Fig. 5 after calibration by zero-point vibrational energy (ZPVE) of the system. Note that the initial structure and final structure in the activation progress are defined as IS and FS.

Using the two equations mentioned above, the adsorption and activation temperatures for this system can be predicted. Thus, the activation of $S_2O_8^{2-}$ to $SO_4^{\bullet-}$ on MoS_2 occurs when the temperature reaches a certain value at the ideal state with the infinite reaction time. In order to obtain more accurate activation performance, the relationship between reaction time (τ) and temperature (*T*) is estimated by the following equation (Jiang et al. 2014):

$$\tau = \frac{1}{\upsilon e^{-\frac{E_{bar}}{k_B T}}} \quad (5)$$

where υ is the frequency of O-O bond of SO_4-O_4S in PDS ($S_2O_8^{2-}$), k_B is the Boltzmann's constant (8.62×10^{-5} eV/K), E_{bar} is energy barrier for $S_2O_8^{2-}$ activation. The values of υ and E_{bar} can be obtained through DFT calculations.

3. Results and discussion

3.1. Evaluation on the effect of temperature for PDS activation in pollutant degradation

Firstly, CBZ degradation in the heat activated PDS process under different temperature by the water bath was tested, shown in Fig. 1(a). It is observed that the removal efficiency of CBZ was enhanced with the increase of the temperature. When the temperature was above 50 °C, CBZ could be completely decomposed in 4 h by the heat activated PDS process. For the PDS can be efficiently activated at 50 °C for almost complete degradation of CBZ, the enhancement on the degradation percentage of CBZ is not obvious when the temperature is above 50 °C. In order to understand the kinetic performance of PDS activation at different temperature, eq. (5) is used to predict the reaction time at different temperature. In eq. (5), the frequency υ of O-O bond of SO_4-O_4S is unknown, which can be determined by frequency calculation here. Fig. 1(b) and 1(c) exhibit the vibration frequencies of O-O along different directions of 20.006 and 23.478 THz, respectively. The average of the two values 21.742 THz is taken as the frequency υ of O-O bond and used in eq. (5). The calculated reaction time at different temperature is shown in Fig. 1(d). As shown, $\tau(T)$ decreases exponentially with *T* increasing. It indicates that the reaction time is 0.165 s at room temperature. When *T* increases to 50 °C, the reaction is facilitated significantly and only needs 0.018 s. In addition, further increasing the temperature above 50 °C, the reaction time does not reduce much. The calculated result is in accordance with the experimental result of heat-activated PDS. It can be seen that the increase of the temperature can strongly improve the rates of PDS activation below 50 °C, in which the rates of PDS activation

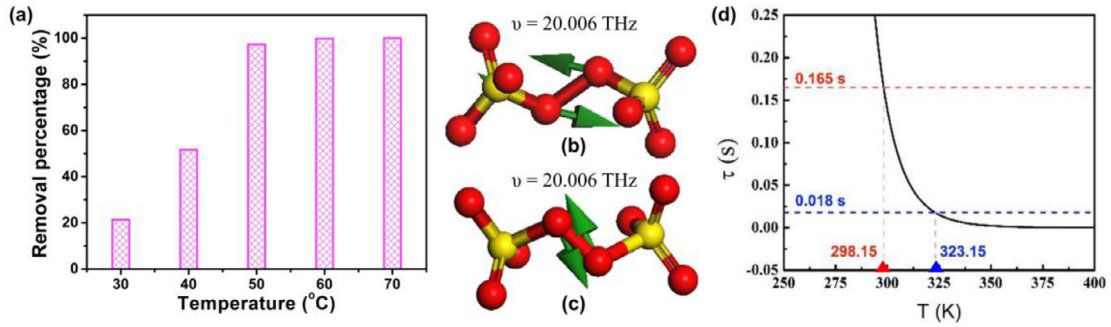

Fig. 1. Removal percentage of CBZ in heat/PDS process under different temperature (from 30 to 70 °C) (a): $[PDS]_0$= 2.0 g L^{-1}, $[CBZ]_0$=10 mg L^{-1}, initial pH 5.0, the frequency of O-O bond in PDS along different directions (b) and (c), temperature dependent reaction time function (d).

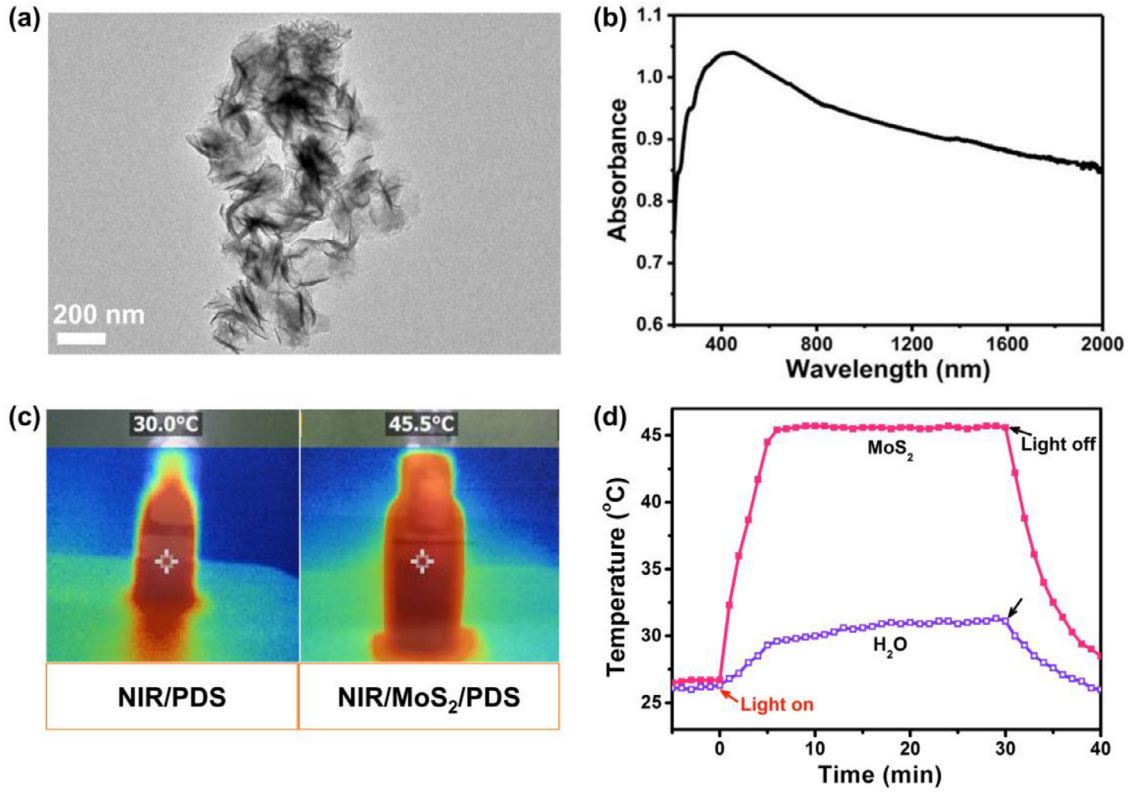

Fig. 2. TEM (a) and UV-vis-NIR-DRS (b) of MoS_2, IR photo of the oxidation processes (c), temperature change of the NIR/MoS_2 process *vs* NIR/H_2O (d): $[MoS_2]_0$=1.0 g L^{-1} and $[distance]_{light\text{-}bottle}$=2 cm.

at 50 °C is 9.2 times to that at room temperature. The result indicated that the PDS could be efficiently activated through increasing the temperature of the solution. Thus, next we take advantage of the MoS_2 materials to transfer light to heat to increase the temperature of solution, which promotes PDS activation for the removal of the pollutants.

3.2. Light-to-heat conversion potential of MoS_2

Then MoS_2 was characterized to evaluate its ability in light-to-heat conversion. As shown in Fig. S2(a), XRD pattern of MoS_2 was obtained. The intense diffraction peaks at 17.6°, 32.9°, 35.9° and 57.5° correspond to the reflection of (011), (100), (103) and (110) planes of MoS_2, respectively, which are all compatible with those reported for MoS_2 in JCPDS card No. 37-1492 standard (Khataee et al. 2018). Fig. 2(a) shows the TEM image of as-prepared MoS_2, which is found that the MoS_2 showed thin 2D structures with lateral dimension dispersions. The XPS spectra of Mo 3d and S 2p are shown in Fig. S2(b) and (c). Two characteristic peaks at 232.6 and 235.7 eV were corresponded to Mo $3d_{5/2}$ and Mo $3d_{3/2}$ respectively as shown in Fig. S2(b). Fig. S2(c) showed that the characteristic peaks at 162.5 and 168.8 eV were corresponded to S $2p_{3/2}$ and S $2p_{1/2}$ respectively. UV–vis diffuse reflectance spectra (DRS) measurement was performed to evaluate the optical response of the catalysts. As shown in Fig. 2(b), MoS_2 exhibits a strong absorption in the entire region of the full solar spectrum from 200 to 2000 nm, which includes UV, visible light and NIR light. The characterization data suggested that as-prepared MoS_2 has good photothermal conversion ability.

To further testify the photothermal conversion ability of MoS_2, infrared camera was used to record the temperatures of the solution under different MoS_2 concentration by NIR irradiation (Fig. 2(c)). The plots of the temperature change were shown in Fig. 2(d) and Fig. S3. It can be seen that the MoS_2 could strongly increase the temperature of the solution. For instance, when the MoS_2 concentrations were 1.0 g L^{-1}, the temperatures of the solution under NIR irradiation reached at 45 °C in 5 min, compared with 30 °C in the absence of MoS_2. Moreover, the temperature of the solution also increased with the increment of MoS_2 concentration. When the MoS_2 concentrations were 0.10, 0.50 and 2.0 g L^{-1}, the temperatures of the solution reached at 38, 40 and 55 °C in 5 min (Fig. S3), respectively. The results suggested that MoS_2 could absorb the energy of NIR to transfer to heat energy for further application. Thus next PDS activation through photo-thermal conversion by MoS_2 under NIR irradiation for pollutant removal is assessed.

3.3. Performance and kinetics of PDS activation by MoS_2 under NIR irradiation

To testify the oxidation potential of the NIR/MoS_2/PDS process, batch experiments are conducted for CBZ degradation in different comparative oxidation processes, including NIR/MoS_2, MoS_2/PDS, NIR/PDS and NIR/MoS_2/PDS processes, respectively. As shown in Fig. 3(a), the photo-catalytic process of MoS_2 under NIR irradiation showed negligible removal of CBZ (<10 %), suggesting that the energy of NIR was unable to stimulate MoS_2 to degrade CBZ by the sole photo-catalytic process without PDS. Meanwhile, MoS_2 alone and NIR alone displayed limited PDS activation ability with the removal percentage of CBZ was 27.7% and 25.7% in MoS_2/PDS and NIR/PDS systems, respectively. Significantly, the removal efficiency of CBZ reached at 81.5% with the whole access of NIR, MoS_2 and PDS. It was observed that the NIR/MoS_2/PDS processes showed much higher CBZ degradation efficiency than those of NIR/MoS_2, MoS_2/PDS and NIR/PDS system, of which was even higher than the sum of the efficiencies for the NIR/MoS_2, MoS_2/PDS and NIR/PDS

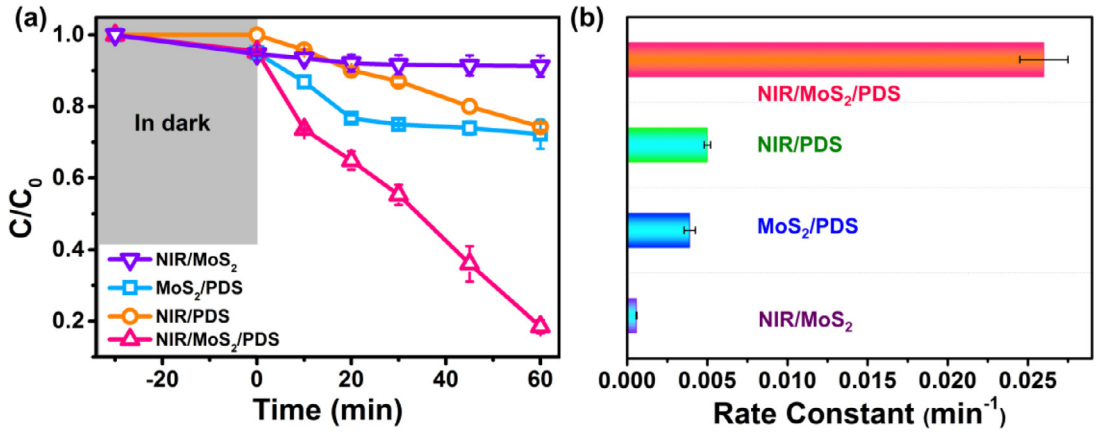

Fig. 3. CBZ degradation (a) and pseudo-first order rate (b) in different comparative oxidation systems: $[PDS]_0$= 2.0 g L^{-1}, $[MoS_2]_0$=1.0 g L^{-1}, $[CBZ]_0$=10 mg L^{-1}, initial pH 5.0, and $[distance]_{light\text{-}bottle}$=2 cm.

systems. The results indicated that there was a joint action between the NIR and MoS_2, which played a synergistic effect on PDS activation for efficient CBZ removal. Considering the characteristics of the NIR irradiation and photo-thermal transformation of MoS_2 material, the joint action between the NIR and MoS_2 would possibly be the effect of light-to-heat conversion. Moreover, the temperature of the MoS_2/PDS, NIR/PDS and NIR/MoS_2/PDS processes were tested as 25, 30 and 45 °C, respectively, which further indicated the light-to-heat conversion effect between NIR and MoS_2 for PDS activation. Thus, the light-to-heat conversion between NIR and MoS_2 played important effect on PDS activation and showed high application potential in pollutants removal. Moreover, the observed pseudo first order rates of the processes were modeled in Fig. 3(b), in which the NIR/MoS_2, NIR/PDS, MoS_2/PDS and NIR/MoS_2/PDS processes were calculated to be 0.001, 0.005, 0.004 and 0.026 min^{-1}, respectively. The observed reaction rate of the NIR/MoS_2/PDS process is 6.5 times to that of the MoS_2/PDS process. According to the calculation result of Fig. 1(d), the temperature of the MoS_2/PDS and NIR/MoS_2/PDS processes are 25 and 45 °C, corresponding with the PDS activation time are 0.165 and 0.027 s, respectively. It is concluded that the activation rate was improved 6.1 times with the assistance of NIR irradiation theoretically, which agrees with the experimental results that the observed rate of NIR/MoS_2/PDS process is 6.5 times to that of the MoS_2/PDS process. It further demonstrated that the light-to-heat activation was the dominant way for PDS activation in the NIR/MoS_2/PDS process. Additionally, the degradation of CBZ in the NIR/MoS_2/PDS process was compared with that in the heat-activated PDS process at 45 °C, shown in Fig. S4. The degradation performance of CBZ in the heat-activated PDS process was slightly higher than that in the NIR/MoS_2/PDS process, in which the observed rate constant of CBZ degradation in the heat-activated PDS process was 2.2 times to that in the NIR/MoS_2/PDS process (insert of Fig. S4). This might attribute to that the heat-activated PDS process was always maintained at 45 °C, while the NIR/MoS_2/PDS process relied on the MoS_2 to absorb the energy from light to achieve 45 °C, whereas the light-to-heat induced PDS activation that largely depended on the photo-thermal transfer ability cannot obtain the activation energy as far as heat-activated PDS process. However, the NIR/MoS_2/PDS process can develop an environmentally friendly way to use the ultimate solar light energy to replace the traditional heating ways by electricity or fuels as well as can simultaneously obtain an efficient pollutants removal performance. These results demonstrated that the MoS_2 could efficiently transfer the light to heat under NIR irradiation to increase the reaction temperature, thus largely enhance the PDS activation rates for fast pollutants degradation.

3.4. Oxidation mechanism of the light-to-heat conversion process

To elucidate the oxidation mechanisms in the different comparative systems, the reactive oxidation species (ROS) were primarily investigated through the radical quenching studies. Fig. 4(a) displayed that the addition of tert-butyl alcohol (TBA) at a molar ratio of 200:1 to PDS concentration largely inhibited the removal efficiency of CBZ, while the methanol (MeOH) at the same molar ratio showed almost complete quenching effect on the CBZ degradation in the NIR/MoS_2/PDS process. The results indicated that the NIR/MoS_2/PDS process was a radical oxidation process that consisted of hydroxyl radicals and sulfate radicals. However, the TBA and MeOH showed little effects on the CBZ degradation in both the MoS_2/PDS and NIR/PDS systems, shown in Fig. S5. The results suggested that the hydroxyl radicals and sulfate radicals were not the main ROS in both MoS_2/PDS and NIR/PDS systems, which was totally inconsistent with the NIR/MoS_2/PDS process. Furthermore, EPR studies were carried out to demonstrate the ROS generated in these oxidation systems, the results are shown in Fig. 4(b). No characteristic peaks of radicals were found in both MoS_2/PDS and NIR/PDS systems. However, in the NIR/MoS_2/PDS process, the signals of DMPO-OH and DMPO-SO_4 were both observed, indicating that, corresponding with the results of quenching studies, the $SO_4^{\bullet-}$ and •OH were generated in the NIR/MoS_2/PDS process.

To reveal the transformation of the $S_2O_8^{2-}$ activation for $SO_4^{\bullet-}$ and •OH generation, PDS activation pathway on MoS_2 was investigated by transition state search calculation, and the result is shown in Fig. 4(c). The lengths of middle O-O bond in IS, TS and FS are 1.481 Å, 2.568 Å and 3.553 Å, respectively. During the activation process, the bond distance is stretched until it breaks to generate two [SO_4^-]. It is found that the corresponding energy barrier for activating $S_2O_8^{2-}$ into [SO_4^-] is 0.743 eV. In addition, the relative energy of FS is 0.449 eV, which is higher than that of IS. This phenomenon demonstrates that $S_2O_8^{2-}$ activation on MoS_2 is not thermodynamically spontaneous. Therefore, external energy, such as heat, is required to overcome the energy barrier for $S_2O_8^{2-}$ activation. In addition, the spin density of FS is calculated to confirm the possible generation of $SO_4^{\bullet-}$ and the result is shown in Fig. 4(d), where shows that the two [SO_4^-] has strong spin state, indicating $S_2O_8^{2-}$ activated into $SO_4^{\bullet-}$ radicals on MoS_2. Therefore, $SO_4^{\bullet-}$ was demonstrated to generate in this PDS activation process. According to the previous studies, the PDS could be activated to generate $SO_4^{\bullet-}$, then $SO_4^{\bullet-}$ could transfer to •OH quickly through the following reaction:

$$SO_4^{\bullet-} + H_2O \rightarrow OH + SO_4^{2-} + H^+ \quad (6)$$

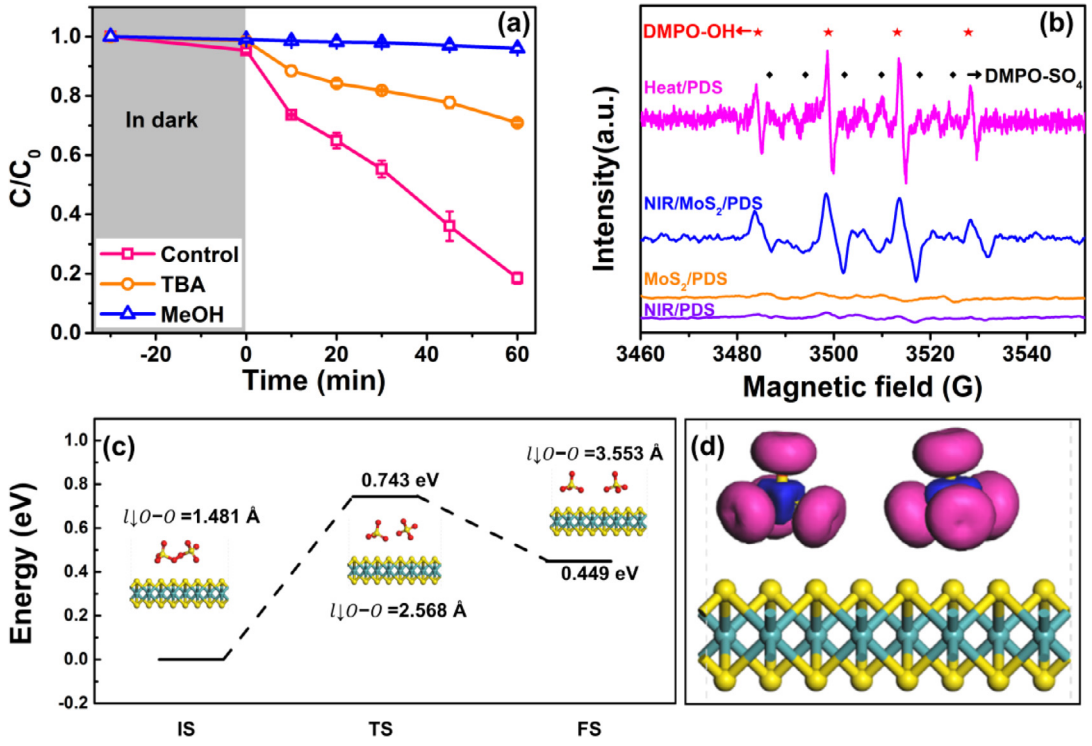

Fig. 4. Scavenging tests (a): MeOH = TBA = 0.74 M and EPR spectra (b) of various oxidation processes: $[PDS]_0$= 2.0 g L^{-1}, $[MoS_2]_0$=1.0 g L^{-1}, $[CBZ]_0$=10 mg L^{-1}, initial pH 5.0, $[distance]_{light\text{-}bottle}$=2 cm, and [DMPO]= 0.10 M. Activation pathway of $S_2O_8^{2-}$ on MoS_2 (c) and spin density of FS, where IS, TS and FS represent initial structure, transition structure and final structure (d), respectively. The red and blue regions in (d) are displayed the different directions of spin: up and down.

According to the results of ROS determination and ROS calculation, the oxidation mechanism of the NIR/MoS_2/PDS process was a radical oxidation process that consisted of hydroxyl radicals and sulfate radicals, which was totally different with the MoS_2/PDS and NIR/PDS systems. Moreover, the ROS in the heat/PDS process at 45 °C was also determined, in which the signals of DMPO-OH and DMPO-SO_4 were found. The results indicated that the oxidation mechanism of the NIR/MoS_2/PDS process was similar to the heat activated PDS process, which further verified the heat activation was the main activation pathway of the NIR/MoS_2/PDS process. Therefore, it was deeply confirmed that the heat generated from light-to-heat conversion between NIR and MoS_2 played important role on PDS activation for pollutants removal. Next DFT calculations are adopted to verify the possibility of the light-to-heat conversion by MoS_2 for PDS activation.

3.5. The difference of Gibbs free energies for PDS activation by MoS_2 at different temperature

It is known that the energy barrier in transition state search calculation is at the condition of 0 K. To take into consideration the effect of temperature, the difference of Gibbs free energies (ΔG) for $S_2O_8^{2-}$ adsorption on MoS_2 and $S_2O_8^{2-}$ activation into $SO_4^{\bullet-}$ as a function of temperature are established with the atomistic thermodynamics described in eq. (3) and (4). $G_{S_2O_8^{2-}}(T)$, $G_{MoS_2}(T)$, $G_{MoS_2-S_2O_8^{2-}}(T)$ and $\Delta G_{adsorption}(T)$ after calibration were plotted in Fig. 5(a) and 5(c), while Fig. 5(b) and 5(d) illustrate the Gibbs free energy for $S_2O_8^{2-}$ activation into $SO_4^{\bullet-}$. The specific values after calibration at different temperatures are listed in Tables S2 and S3 of Supporting information. The results show that $G_{S_2O_8^{2-}}(T)$, $G_{MoS_2}(T)$, $G_{MoS_2-S_2O_8^{2-}}(T)$ and $\Delta G_{adsorption}(T)$ decreases as T increases, and $\Delta G_{adsorption}$ becomes negative at T_{ads} = 38.82 K, where T_{ads} acquired by linear fitting method based on the obtained $\Delta G_{adsorption}(T)$ values is defined as the adsorption temperature. Fig. 5(c) indicates that the $S_2O_8^{2-}$ can be adsorbed on MoS_2 above 38.82 K (Table S4). In addition, $\Delta G_{activation}(T)$ changes from positive value to negative value at 44.99 K as shown in Fig. 5(d). However, it turns positive and remains increasing exponentially after 1107.55 K. The activation temperature is represented by T_{act}. It shows that the activation reaction of $S_2O_8^{2-}$ activation to $\bullet SO_4^-$ on MoS_2 can occur at 44.99 K$<T_{act}<$ 1107.55 K. Note that $\Delta G_{activation}$ reaches minimum at ~500K, demonstrating the strongest driving force for the activation reaction. In addition, $\Delta G_{activation}$ changes slightly between 300~800K, which indicates relatively stable activation performance of MoS_2 at a wide temperature range. However, this reaction is at aqueous condition, water solution is boiling at 373K, i.e. $S_2O_8^{2-}$ activation reaction has optimum performance at 300~373 K. Based on above results, it can be known that the $S_2O_8^{2-}$ activation to $SO_4^{\bullet-}$ on MoS_2 is thermodynamically feasible at the temperature higher than 44.99 K, and optimum at 300~373 K. In this experiment, the MoS_2 could absorb the NIR light to increase the temperature of the solution to 318K, which reached the optimum temperature range of PDS activation by MoS_2. The results indicated that the MoS_2 could absorb the NIR light to improve the temperature of the solution to decrease the energy gap of PDS activation and thus promote PDS activation performance by MoS_2. The above results and discussion demonstrated that the possibility of the light-to-heat conversion to enhance PDS activation for pollutants by NIR irradiation. The overall mechanism is illustrated in Scheme 1. Then the experiments under sunlight are conducted to further evaluate the practical application potential of the light-to-heat conversion enhanced PDS activation process.

3.6. Practical application of the light-to-heat conversion enhanced PDS activation process

The pollutants can be rapidly degraded in the heterogeneous NIR/MoS_2/PDS process. However, the highly dispersed suspension is hard to reuse and may induce secondary pollution. Thus we

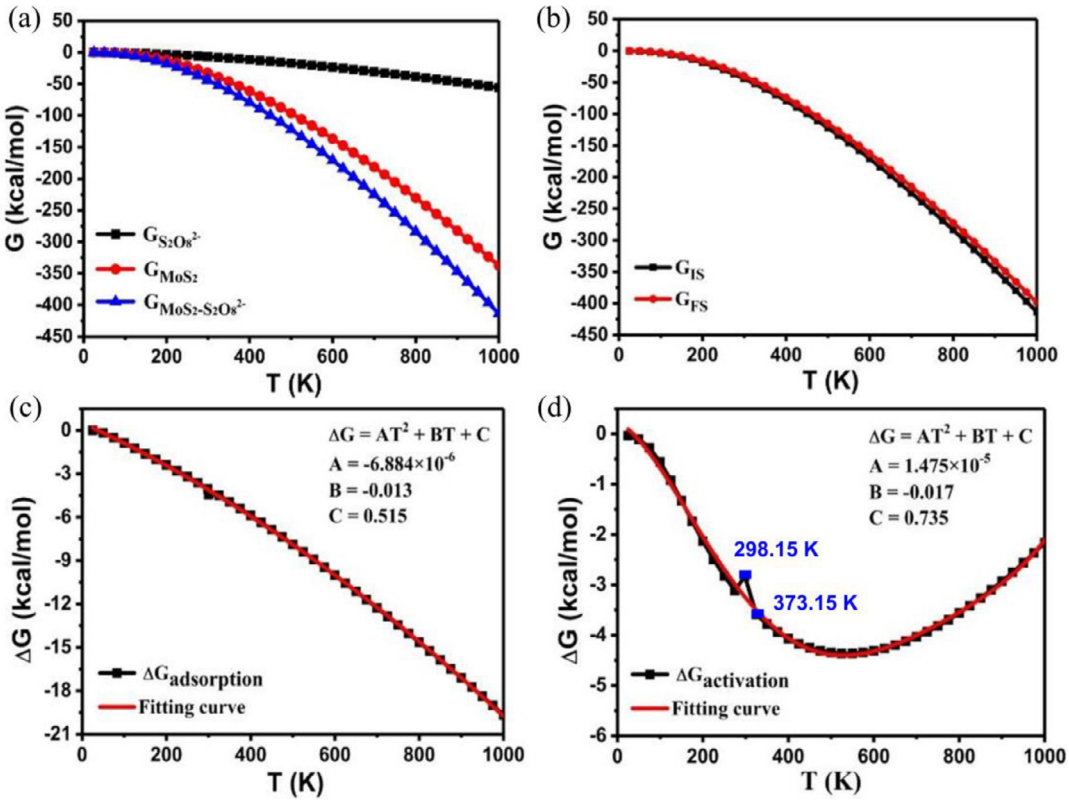

Fig. 5. The temperature dependent Gibbs free energy for $S_2O_8^{2-}$ adsorption on MoS_2 (a) and subsequent activation (b), the Gibbs free energy difference and fitting curve for adsorption (c) and activation (d).

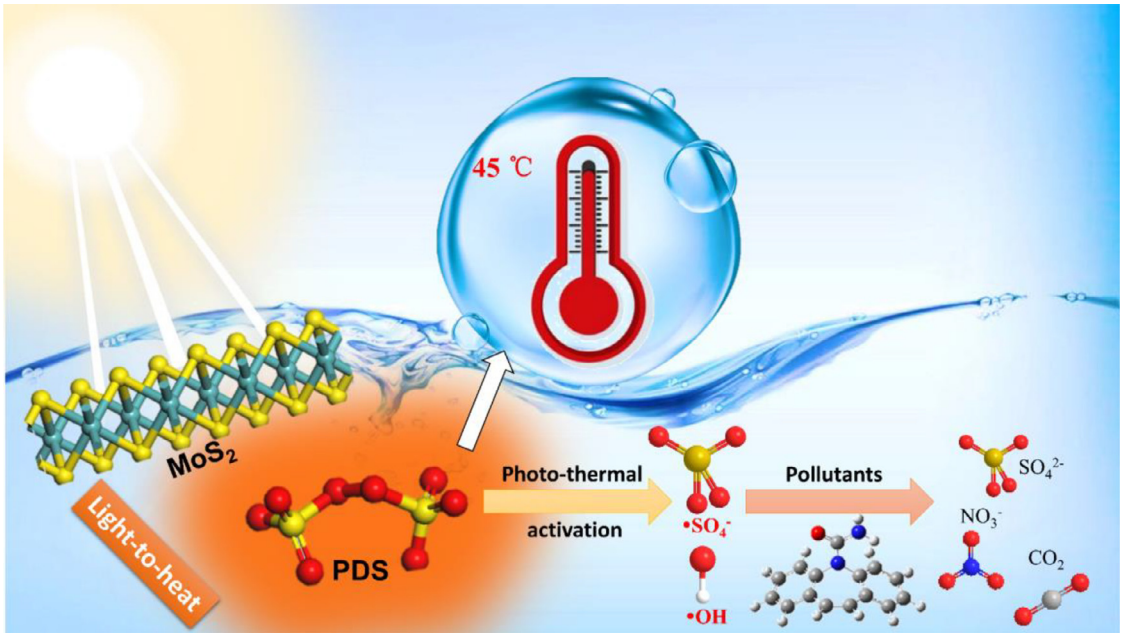

Scheme 1. Proposed mechanism of the light-to-heat conversion to enhance PDS activation by NIR irradiation for pollutants removal.

considered to assemble the MoS_2 nanosheets into the CC for recycling. An experiment on the degradation of methylene blue (MB) by the CC/MoS_2-PDS system under sunlight irradiation was conducted to testify the practical application potential of the light-to-heat conversion for pollution control. The MoS_2 nanosheets were grown on the highly flexible surface of CC with diameter of 5 cm using a facile solvothermal method to form a CC/MoS_2 membrane. As shown in the SEM image of the CC/MoS_2 membrane (Fig. 6(a)), the crimped MoS_2 nanosheet with high density were grown on the surface of CC, forming a 3D hierarchical shape. Higher-magnification SEM image from Fig. 6(b) and Fig. S6 displayed that numerous MoS_2 nanosheets were grown on the surface of CC compared with the raw CC (Fig. 6(c)), which enabled the CC/MoS_2 membrane to afford active sites for efficiently transferring the light to heat energy. The photo of raw CC, fresh CC/MoS_2 membrane and used CC/MoS_2 membrane were displayed in Fig. 6(d)-

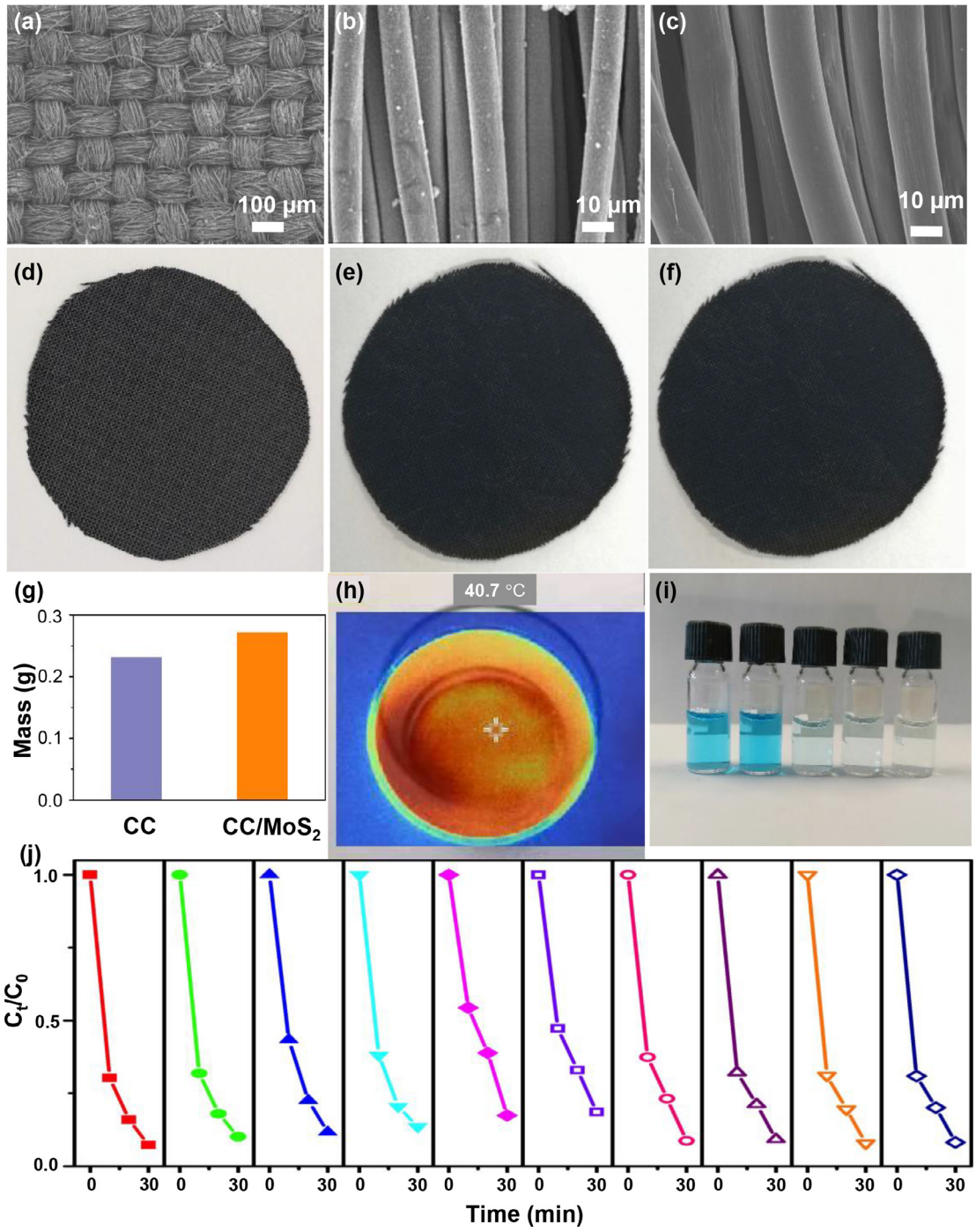

Fig. 6. SEM images of primary of CC/MoS_2 (a) and high-magnification SEM of CC/MoS_2 (b) and CC (c), photo of CC (d), fresh CC/MoS_2 (e) and used CC/MoS_2 (f), mass of CC and CC/MoS_2 (g), IR photo of the solution with CC/MoS_2 under sunlight irradiation (h), MB decolorization in the solution with CC/MoS_2 under sunlight irradiation (i), and cycle experiments on the MB decolorization in the solution with CC/MoS_2 under sunlight irradiation (j): $[PDS]_0$= 2.0 g L^{-1}, $[MB]_0$=10 mg L^{-1}.

(f), while the mass of the raw CC and the fresh CC/MoS_2 membrane was shown in Fig. 6(g), indicating the successful growing of MoS_2 on the surface of CC. 20 mL of the MB solution at 10 mg L^{-1} and PDS were added in a quartz beaker. After placing the CC/MoS_2 membrane, the beaker was taken under the sunlight with light intensity at about 50 mW cm^{-2} to start the experiment. The temperature of the solution is about 41 °C (Fig. 6(h)). It can be seen that the MB could be efficiently decolorized (Fig. 6(i)). The CC/MoS_2 membrane was reused for MB degradation (Fig. 6(j)). Results showed the CC/MoS_2 membrane can be easily recycled and reused and stably remove the MB even in 10 cycles, which would not cause high cost and secondary contamination to the environment. This superior decolorization of MB should be primarily ascribed to the high light-to-heat transfer ability of the CC/MoS_2 membrane to improve the reaction temperature to efficiently activate PDS to generate radicals. Based on the high removal efficiency, stability, and low cost, we propose that the light-to-heat induced PDS activation process is an ideal system to degrade organic con-

taminants for environmental remediation and solar energy application.

4. Conclusion

In summary, the utilization of renewable solar energy via light-driven thermocatalysis offers a potential alternative strategy for environmental remediation. The MoS_2 could efficiently absorb the energy of light, resulting in light-to-heat conversion, thereby increasing reaction temperature for driving the PDS activation in the removal of pollutants. After the light-to-heat conversion, the oxidation ability of Fenton-like processes was largely improved. The potential of the light-to-heat conversion application in the PDS activation and its oxidation mechanism are deeply elucidated from the view point of both experimental and theoretical aspects, which offers the foundation and direction for the future research on the light-to-heat conversion application in the Fenton-like or other oxidation processes. However, the light-to-heat induced PDS activation largely depended on the photo-thermal transfer ability of the materials. Even though the MoS_2 can absorb the energy from light to transfer to heat, the transfer efficiency and rate are not high enough to achieve the comparable performance of that in the heat-activated PDS process. Thus, in the future study, we will take effort in coupling a good catalyst with strong absorption of light to heat to produce much enhancement in the degradation of organic pollutants. The light-to-heat induced Fenton-like oxidation process should be an ideal oxidation system to degrade organic contaminants for environmental remediation and solar energy application. It is anticipated that this work may enable the wide development of the solar energy application to open up a novel strategy for environmental purification.

Declaration of Competing Interest

The authors declare that they have no known competing financial interests or personal relationships that could have appeared to influence the work reported in this paper.

Acknowledgements

The present study was financially supported by the Guangdong Basic and Applied Basic Research Foundation (Nos. 2020B1515020038 and 2019A1515111088), National Natural Science Foundation of China (No. 21777033), China Postdoctoral Science Foundation (No. 55350333), the Pearl River Talent Recruitment Program of Guangdong Province (No. 2019QN01L148) and Science and Technology Planning Project of Guangdong Province (No. 2017B020216003).

Supplementary materials

Supplementary material associated with this article can be found, in the online version, at doi:10.1016/j.watres.2020.116720.

References

Ao, Z., Li, S., Jiang, Q., 2009. Thermal stability of interaction between the CO molecules and the Al doped graphene. Phys. Chem. Chem. Phys. 11 (11), 1683–1687.
Ao, Z., Yang, J., Li, S., Jiang, Q., 2008. Enhancement of CO detection in Al doped graphene. Chem. Phys. Lett. 461 (4-6), 276–279.
Avetta, P., Pensato, A., Minella, M., Malandrino, M., Maurino, V., Minero, C., Hanna, K., Vione, D, 2015. Activation of persulfate by irradiated magnetite: implications for the degradation of phenol under heterogeneous photo-Fenton-like conditions. Environ. Sci. Technol. 49 (2), 1043–1050.
Chou, S., Kaehr, B., Kim, J., Foley, B., De, M., Hopkins, P.E., Huang, J., Brinker, C., Dravid, V., 2013. Chemically exfoliated MoS_2 as near-infrared photothermal agents. Angew. Chem. Int. Ed. 52 (15), 4160–4164.
Chu, C., Yang, J., Huang, D., Li, J., Wang, A., Alvarez, P.J.J., Kim, J.-H., 2019. Cooperative pollutant adsorption and persulfate-driven oxidation on hierarchically ordered porous carbon. Environ. Sci. Technol. 53 (17), 10352–10360.
Delley, B., 1990. An all-electro numerical method for solving the density functional for polyatomic moleculles. J. Chem. Phys. 92 (1), 508–517.
Delley, B., 2000. From molecules to solids with the $DMol^3$ approach. J. Chem. Phys. 113 (18), 7756–7764.
Du, A., Sanvito, S., Li, Z., Wang, D., Jiao, Y., Liao, T., Sun, Q., Ng, Y., Zhu, Z., Amal, R., Smith, S.C., 2012. Hybrid graphene and graphitic carbon nitride nanocomposite: gap opening, electron-hole puddle, interfacial charge transfer, and enhanced visible light response. J. Am. Chem. Soc. 134 (9), 4393–4397.
Duan, X., Ao, Z., Zhang, H., Saunders, M., Sun, H., Shao, Z., Wang, S., 2018. Nanodiamonds in sp2/sp3 configuration for radical to nonradical oxidation: Core-shell layer dependence. Appl. Catal. B: Environ. 222, 176–181.
Fan, Y., Ji, Y., Kong, D., Lu, J., Zhou, Q., 2015. Kinetic and mechanistic investigations of the degradation of sulfamethazine in heat-activated persulfate oxidation process. J. Hazard. Mater. 300, 39–47.
Hammer, B., Hansen, L.B., Nørskov, J.K., 1999. Improved adsorption energetics within density-functional theory using revised Perdew-Burke-Ernzerhof functionals. Am. Phys. Soc. 59, 7413–7421.
Hodges, B., Cates, E., Kim, J., 2018. Challenges and prospects of advanced oxidation water treatment processes using catalytic nanomaterials. Nat. Nanotechnol. 13 (8), 642–650.
Jiang, Q., Ao, Z., Li, S., Wen, Z., 2014. Density functional theory calculations on the CO catalytic oxidation on Al-embedded graphene. RSC Adv. 4 (39), 20290–20296.
Kang, J., Zhou, L., Duan, X., Sun, H., Ao, Z., Wang, S., 2019. Degradation of cosmetic microplastics via functionalized carbon nanosprings. Matter 1 (3), 745–758.
Ke, Q., Shi, Y., Liu, Y., Chen, F., Wang, H., Wu, X., Lin, H., Chen, J., 2019. Enhanced catalytic degradation of bisphenol A by hemin-MOFs supported on boron nitride via the photo-assisted heterogeneous activation of persulfate. Sep. Purif. Technol. 229, 115822.
Khataee, A., Eghbali, P., Irani-Nezhad, M., Hassani, A., 2018. Sonochemical synthesis of WS_2 nanosheets and its application in sonocatalytic removal of organic dyes from water solution. Ultrason. Sonochem. 48, 329–339.
Lee, J., von Gunten, U., Kim, J., 2020. Persulfate-based advanced oxidation: critical assessment of opportunities and roadblocks. Environ. Sci. Technol. 54 (6), 3064–3081.
Li, J., Cai, S., Yu, E., Weng, B., Chen, X., Chen, J., Jia, H., Xu, Y., 2018. Efficient infrared light promoted degradation of volatile organic compounds over photo-thermal responsive Pt-rGO-TiO_2 composites. Appl. Catal. B: Environ. 233, 260–271.
Li, R., Zhang, L., Shi, L., Wang, P., 2017. MXene Ti_3C_2: An effective 2D light-to-heat conversion material. ACS nano 11 (4), 3752–3759.
Liao, T., Sun, C., Du, A., Sun, Z., Hulicova-Jurcakova, D., Smith, S., 2012. Charge carrier exchange at chemically modified graphene edges: A density functional theory study. J. Mater. Chem. 22 (17), 8321–8326.
Liu, F., Zeng, M., Li, Y., Yang, Y., Mao, M., Zhao, X., 2016. UV-vis-infrared light driven thermocatalytic activity of octahedral layered birnessite nanoflowers enhanced by a novel photoactivation. Adv. Funct. Mater. 26 (25), 4518–4526.
Liu, T., Wang, C., Gu, X., Gong, H., Cheng, L., Shi, X., Feng, L., Sun, B., Liu, Z., 2014. Drug delivery with PEGylated MoS_2 nano-sheets for combined photothermal and chemotherapy of cancer. Adv. Mater. 26 (21), 3433–3440.
Mombrú, D., Faccio, R., Mombrú, Á.W., 2018. Possible doping of single-layer MoS_2 with Pt: A DFT study. Appl. Surf. Sci. 462, 409–416.
Nie, C., Dai, Z., Meng, H., Duan, X., Qin, Y., Zhou, Y., Ao, Z., Wang, S., An, T., 2019. Peroxydisulfate activation by positively polarized carbocatalyst for enhanced removal of aqueous organic pollutants. Water Res. 166, 115043.
Niu, T., Cai, J., Shi, P., Zhao, G., 2020. Unique electrochemical system for in situ $SO_4^{\bullet-}$ generation and pollutants degradation. Chem. Eng. J. 386, 123971.
Perdew, J., Burke, K., Ernzerhof, M., 1996. Generalized gradient approximation made simple. Phys. Rev. Lett. 77 (18), 3865–3868.
Segall, M., Lindan, P., Probert, M., Pickard, C., Hasnip, P., Clark, S., Payner, M., 2002. First-principles simulation: ideas, illustrations and the CASTEP code. J. Phys.: Condens. Matter 14, 2717–2744.
Wacławek, S., Lutze, H., Grübel, K., Padil, V., Černík, M., Dionysiou, D., 2017. Chemistry of persulfates in water and wastewater treatment: A review. Chem. Eng. J. 330, 44–62.
Waldemer, R., Tratnyek, P., Johnson, R., Nurmi, J., 2007. Oxidation of chlorinated ethenes by heat-activated persulfate: kinetics and products. Environ. Sci. Technol. 41 (3), 1010–1015.
Wang, J., Li, Y., Deng, L., Wei, N., Weng, Y., Dong, S., Qi, D., Qiu, J., Chen, X., Wu, T., 2017. High-performance photothermal conversion of narrow-bandgap Ti_2O_3 nanoparticles. Adv. Mater. 29 (3), 1603730.
Yin, R., Guo, W., Ren, N., Zeng, L., Zhu, M., 2020. New insight into the substituents affecting the peroxydisulfate nonradical oxidation of sulfonamides in water. Water Res. 171, 115374.
Yin, R., Guo, W., Wang, H., Du, J., Zhou, X., Wu, Q., Zheng, H., Chang, J., Ren, N., 2018. Enhanced peroxymonosulfate activation for sulfamethazine degradation by ultrasound irradiation: Performances and mechanisms. Chem. Eng. J. 335, 145–153.
Yin, R., Guo, W., Wang, H., Du, J., Wu, Q., Chang, J, Sand Ren, N., 2019. Singlet oxygen-dominated peroxydisulfate activation by sludge-derived biochar for sulfamethoxazole degradation through a nonradical oxidation pathway: Performance and mechanism. Chem. Eng. J. 357, 589–599.

Zhao, X., Bo, M., Huang, Z., Zhou, J., Peng, C., Li, L., 2018. Heterojunction bond relaxation and electronic reconfiguration of WS_2- and MoS_2-based 2D materials using BOLS and DFT. Appl. Surf. Sci. 462, 508–516.

Zheng, H., Bao, J., Huang, Y., Xiang, L., Faheem, Ren, B., Du, J. M.N., Nadagouda, Dionysiou, D.D, 2019. Efficient degradation of atrazine with porous sulfurized Fe_2O_3 as catalyst for peroxymonosulfate activation. Appl. Catal. B: Environ. 259, 118056.

Zhou, Z., Liu, X., Sun, K., Lin, C., Ma, J., He, M., Ouyang, W., 2019. Persulfate-based advanced oxidation processes (AOPs) for organic-contaminated soil remediation: A review. Chem. Eng. J. 372, 836–851.